ELSEVIER

Current Applied Physics 2 (2002) 525–531

Current Applied Physics
Physics, Chemistry and Materials Science

www.elsevier.com/locate/cap

Derivation of tensile flow properties of thin films using nanoindentation technique

Jeong-Hoon Ahn [a], Eun-chae Jeon [a], Yeol Choi [b,*], Yun-Hee Lee [a], Dongil Kwon [a]

[a] *School of Materials Science and Engineering, Seoul National University, Seoul 151-742, South Korea*
[b] *FRONTICS Inc., Research Institute of Advanced Materials, Seoul National University, Seoul 151-742, South Korea*

Received 27 March 2001; accepted 19 December 2001

Abstract

By regarding the tip blunting as a ball indentation at very low depth range (within about 80 nm in our experiments), the flow properties of Au thin films were derived from the indentation load–depth curve obtained by nanoindentation technique. The effects of pile-up or sink-in were considered in determining the real contact between the indenter and the specimen. The representative strain in indentation was defined in various ways and examined by comparing the flow properties derived from indentation load–depth curve with those measured by tensile test. The best definition was found to be the shear strain at contact edge multiplied by 0.1. When we considered the effects of pile-up or sink-in, the representative stress in indentation could also be determined, and was found to be one third of the mean contact pressure for fully plastic regime. As a more intrinsic property than hardness, the yield strengths of Au films with thickness of 0.56 and 0.99 μm were extrapolated from the derived true stress–true strain curve as 261 ± 30 and 154 ± 18 MPa, respectively.

Keywords: Nanoindentation technique; Au thin film; Pile-up/sink-in; Flow properties

1. Introduction

Nanoindentation technique is one of the most popular methods to evaluate the mechanical properties of small volumes such as thin films due to its simplicity and easiness [1–3]. It records the indentation depth continuously with indentation load, while conventional hardness tests observe the residual imprint as a contact area using an optical microscope. This depth-sensing ability of nanoindenter enables us to evaluate various mechanical properties such as creep [4,5], fracture strength or toughness [6,7], adhesion [8–10] as well as hardness and elastic modulus. Hardness is usually defined as the mean contact pressure between the indenter and the specimen, and it has been used for qualitative comparison of material strengths.

The interpretation of indentation load–depth curve is very ambiguous because of complex indentation stress fields beneath the indenter. In addition, hardness itself is not a basic material property for indicating the material strength [11,12]. In other words, hardness is affected by the elastic and plastic properties of material, the indenter shape, and partially by the experimental procedure and the surface condition of specimen. Accordingly, many attempts have been tried to get more intrinsic properties from indentation tests such as yield [13–17] or tensile strength [18] and even flow properties [19–24].

In this study, both the elastic deflection and the pile-up/sink-in are considered in determining the real contact area between the indenter and the specimen. The modeling of deriving the true stress–true strain curve from indentation load–depth curve is established, especially focused on various definitions of strain in indentation. In experiments, some bulk materials are tested in advance to examine the proposed model by comparing the derived flow properties with those measured directly by uni-axial tensile test. The flow properties of Au thin films are evaluated using nanoindentation technique after the shape of indenter tip is carefully calibrated using a standard sample.

* Corresponding author.
E-mail address: yariman@snu.ac.kr (Y. Choi).

1567-1739/02/$ - see front matter
PII: S1567-1739(02)00155-4

2. Theoretical analysis

Material response during indentation depends on the indenter shape. For a ball indenter, it is divided into the three regimes [13,19,21] shown in Fig. 1: elastic, elastic–plastic, and fully plastic. As the ball indenter penetrates into the specimen, the average strain beneath the indenter increases, as does the mean contact pressure. This increase makes it possible to derive the flow properties of material using ball indentation technique.

2.1. Analysis of indentation load–depth curve

The contact depth h_c between the indenter and the specimen can be obtained by analyzing the unloading curve, which corresponds to elastic recovery during unloading. In the case of perfectly elastic response during indentation, shown in Fig. 2(a), there is no residual imprint and h_c at maximum load equals half of the maximum indentation depth h_{max} [25]. On the contrary, in the case of perfectly plastic response, shown in Fig. 2(c), h_c is equal to h_{max}. But this correlation is true only when the effect of pile-up is not considered.

The indentation load–depth curve for elastic–plastic response is schematically shown in Fig. 2(b). The contact area A will be obtained in this more general case by considering both the elastic deflection and the pile-up during indentation. The elastic deflection depth h_d is calculated by analyzing the unloading curve, whose initial slope is the stiffness S. By extrapolating this tangent line to zero load, the intercept depth h_i is defined. If there is no change in contact area during unloading, as occurs in flat punching, h_d will be $h_{max} - h_i$ [1]. If the shape of indenter is taken into account, h_d will be obtained as [2]

$$h_d = \omega(h_{max} - h_i). \quad (1)$$

Here, ω is a constant dependent on the indenter shape; 1 for a flat punch, 0.72 for a conical indenter, and 0.75 for a paraboloid of revolution.

The contact area A has usually been calculated using the geometrical relationship between h_c^* and A by de-

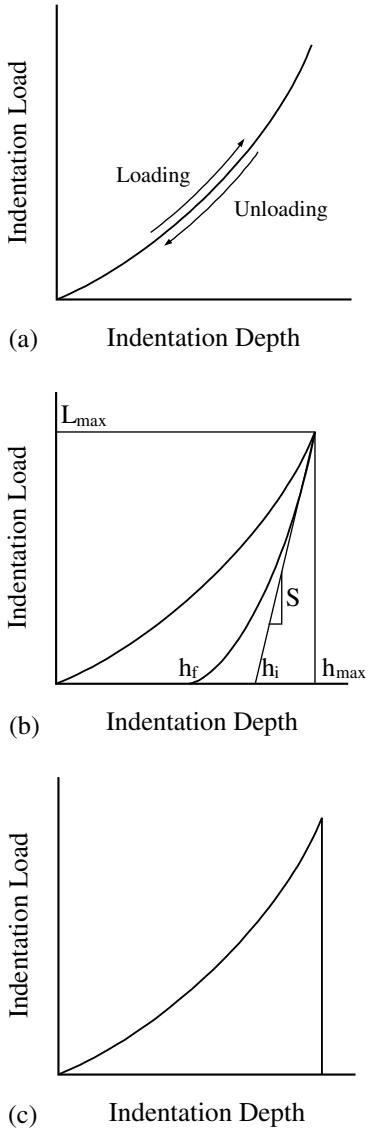

Fig. 2. Typical indentation load–depth curves for (a) elastic, (b) elastic–plastic and (c) plastic responses.

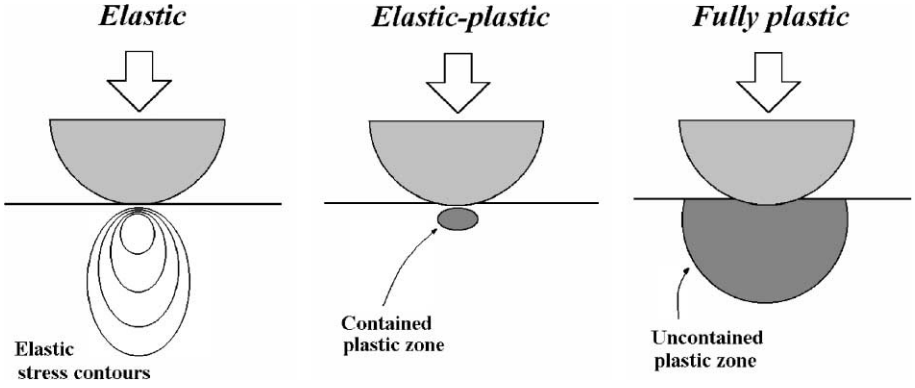

Fig. 1. Schematic representation of plastic zone expansion during ball indentation: elastic, elastic–plastic, and fully plastic regimes [19].

fining $h_c^* = h_{max} - h_d$. Here, superscript $*$ means that the effect of pile-up/sink-in is not included. However, the pile-up/sink-in behavior around indentation alters the actual contact area [21,26,27]. If pile-up occurs, the actual contact area will be larger than expected, and if sink-in occurs, the actual contact area will be smaller than expected. It is well established that the extent of this pile-up/sink-in is determined by a dimensionless constant c for metals with low yield strain [27]

$$c^2 = \frac{a^2}{a^{*2}} = \frac{5}{2}\frac{2-n}{4+n}, \tag{2}$$

where a is the contact radius and n is the work-hardening exponent of material. This equation means that the dominant factor affecting the shape and size of plastic zone during indentation for metals is the work-hardening exponent. In detail, if the plastic zone beneath the indenter is large for small n, the surrounding elastic zone cannot afford to accommodate the volume change due to the indenter penetration, so that the pile-up will occur.

By combining Eqs. (1) and (2), the contact radius considering both the elastic deflection and the pile-up/sink-in can be obtained as

$$a^2 = \frac{5}{2}\frac{2-n}{4+n}\left(2Rh_c^* - h_c^{*2}\right), \tag{3}$$

where R is the indenter radius. This equation means that the prediction of unknown n or another parameter related to pile-up is necessary to determine the actual contact radius from the measured indentation load–depth curve. In our study, this parameter is determined using the modeling proposed in the following section.

Elastic modulus E can be obtained from the stiffness S using the relation [28]

$$S = \beta\frac{2}{\sqrt{\pi}}E_r\sqrt{A}, \tag{4}$$

where

$$\frac{1}{E_r} = \frac{1-\nu_i^2}{E_i} + \frac{1-\nu^2}{E}.$$

Here, E_r is the reduced modulus and β is a numerical factor; $\beta = 1$ for a circular indenter, $\beta = 1.012$ for a square indenter, and $\beta = 1.034$ for a triangular indenter. And, ν is Poisson's ratio, and subscript i means the indenter.

2.2. Derivation of true stress–true strain curve

Looking in detail at the three regimes occurring during ball indentation, the mean contact pressure increases as follows [13]. For the initial elastic regime, the mean contact pressure increases linearly with the square root of the indentation load. When the mean contact pressure reaches the elastic limit, the plastic zone will develop beneath the indenter as shown in Fig. 1. In the elastic–plastic regime, the mean contact pressure increases gradually. After the plastic zone expands to the surface of specimen, the mean contact pressure increases slightly due to work-hardening characteristics. This increase makes it possible to derive the plastic flow properties of material in the fully plastic regime.

Several methods are used to define the representative strain ε_R in indentation. First, ε_R has been usually defined as [13]

$$\varepsilon_R = K_1\frac{a}{R} = K_1\sin\gamma. \tag{5}$$

Here, K_1 is about 0.2 and γ is a contact angle between the indenter and the specimen as shown in Fig. 3. This equation is based on the experimental results obtained using the traditional optical technique. A similar definition has also been proposed by considering the work-hardening characteristics [26]; $\varepsilon_R = 0.28(1+1/n)^{-n}a/R$, where the constant corresponding to K_1 varies slightly from 0.17 to 0.19.

Second, ε_R can be defined as the average shear strain using the relation [17,29]

$$\varepsilon_R = K_2\frac{h_c}{a}. \tag{6}$$

This equation can also be derived from Eq. (4) using the relation $a^2 \approx 2Rh_c$ for shallow indentation, and K_2 is about 0.4.

Third, ε_R can be defined as the average plastic strain in depth direction by analyzing the area change during indentation. For the fully plastic regime where the elastic deformation is negligible, the average strain in depth direction can be obtained as

$$\varepsilon_{zz} = -\left(\varepsilon_{xx} + \varepsilon_{yy}\right) = -\int_{S1}^{S2}\frac{dS}{S}, \tag{7}$$

where $S1$ is the initial area and $S2$ is the area changed by indentation as shown in Fig. 3. Hence,

$$\varepsilon_R = -\varepsilon_{zz} = \ln\frac{2}{1+\cos\gamma}. \tag{8}$$

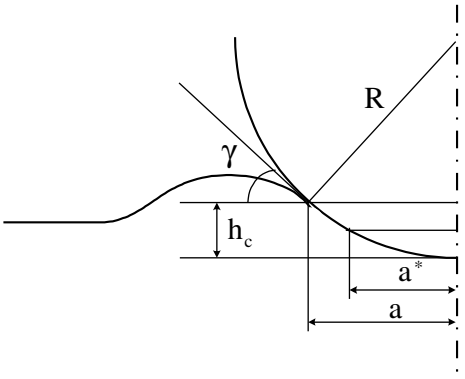

Fig. 3. Schematic representation of pile-up phenomenon.

As a comparison, for a Vickers indenter, ε_R is constant regardless of indentation depth, i.e., $\varepsilon_R = -\ln\cos\gamma \approx 0.076$ [30].

Finally, the strain distribution under the indenter can be calculated using the displacement in depth direction u_z. For a ball indenter,

$$u_z = h - \left(R - \sqrt{R^2 - r^2}\right). \tag{9}$$

By differentiating,

$$\varepsilon_{zr} = \frac{\partial u_z}{\partial r} = -\frac{1}{\sqrt{1-(r/R)^2}}\frac{a}{R}. \tag{10}$$

ε_R can then be defined by setting $r = a$ and multiplying a constant α:

$$\varepsilon_R = \frac{\alpha}{\sqrt{1-(a/R)^2}}\frac{a}{R} = \alpha\tan\gamma. \tag{11}$$

Here, $\tan\gamma$ is the shear strain at contact edge.

Next, the representative stress σ_R can be obtained from the mean contact pressure P_m. In the elastic regime, the value of P_m/σ_R ratio increases linearly up to about 1.1. It increases gradually through the elastic–plastic regime, and is almost constant in the fully plastic regime [13,19]:

$$\frac{P_m}{\sigma_R} = \Psi. \tag{12}$$

Here, Ψ is expected to have some relationship with plastic-zone expansion, i.e., the yield strain and the work-hardening exponent, and will be discussed later.

3. Experimental procedures

The bulk specimens such as AISI1025, SA106, and thermo-mechanical-control-process (TMCP) steels were used to examine our modeling. The surface of bulk specimen was finally polished with 1 μm Al_2O_3 powder, and another specimen for tensile test was fabricated as a cylinder type with 25 mm gauge length and 6 mm diameter. Au films were deposited using E-gun evaporator and their thickness values were determined as 0.56 and 0.99 μm by scanning electron microscope observation.

Two types of indentation system were used: an Advanced Indentation System by FRONTICS Inc. as a microindenter and a TriboScope Nanomechanical system by HYSITRON Inc. as a nanoindenter. The microindenter consists of a 300 kgf loadcell, and a linear variable displacement transducer (LVDT) with resolution of 0.2 μm. The nanoindenter contains a three-plate capacitive force/displacement transducer, which provides load resolution of 100 nN and depth resolution of 0.2 nm. In the case of the microindenter, to minimize the error caused by system compliance, the indenter and the LVDT were placed as closely together as possible. The indenter was a WC ball of 0.5 mm radius, and indentation speed was 0.1 mm/min. In the case of the nanoindenter, the system compliance was carefully calibrated using a fused quartz as a standard sample. The indenter was a diamond cone indenter with 60° apex angle, which was carefully calibrated using the fused quartz to determine the tip radius. Indentation speed was 100 μN/s at maximum load of 500 μN and 2500 μN/s at maximum loads of more than 1250 μN. In addition, the true stress–true strain curves of the bulk specimens were directly measured by tensile test at cross-head speed of 1 or 2 mm/min.

4. Results and discussion

The measured indentation load–depth (P–h) curves of bulk specimens (AISI1025, SA106, and TMCP steels), and Au films, are shown in Fig. 4. For each specimen, more than five curves were measured. Their reproducibility was excellent except for Au film with thickness of

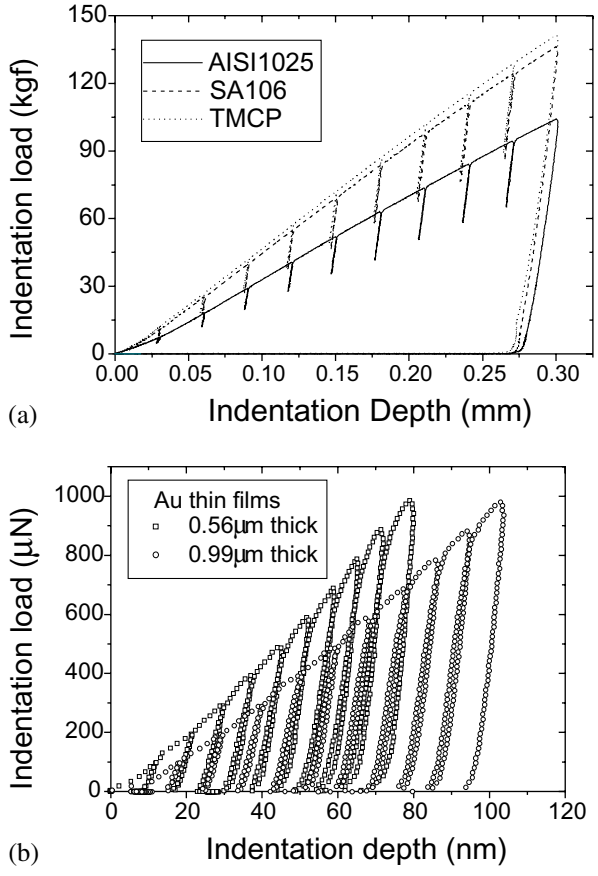

Fig. 4. Measured P–h curves of (a) AISI1025, SA106, SA213 and (b) Au films with thickness of 0.56 and 0.99 μm.

0.99 μm—perhaps due to the indenter sliding caused by the larger surface roughness of thicker Au film.

In analyzing P–h curves, we first calculated the elastic deflection at each indentation depth. The unloading curve follows the equation [2]

$$P = k(h - h_f)^m, \tag{13}$$

where k and m are material constants. By differentiating P with h and putting $h = h_{\max}$, we obtained the stiffness and then calculated the elastic deflection depth.

To consider the change of contact area due to pile-up/sink-in, the work-hardening exponent n was calculated using the iteration method. Using an initial value of n as 0.3, we could obtain the true stress–true strain (σ_R–ε_R) relation through the analysis proposed in Section 2.2. Then, the value of n was modified using the Hollomon equation $\sigma_R = K\varepsilon_R^n$. By iterating this procedure until the input value equaled the return value, the final value of n was achieved.

The flow properties derived from indentation load–depth curve and those measured by tensile test are shown together in Fig. 5. Of various definitions of strain proposed in Section 2.2, i.e., Eqs. (5), (6), (9), and (12), Eq. (12) shows the best agreement. In other words, the shear strain at contact edge multiplied by 0.1 can successfully predict the work-hardening characteristics of the proposed materials with various n. Compared with strain definitions in terms of a/R or h/a, it changes more sharply and describes more exactly the extent of deformation beneath the indenter in our study. In the case of strain definition as an average plastic strain in depth direction, i.e., Eq. (9), the average plastic strain cannot predict well the work-hardening characteristics while it has an advantage of no need for an experimentally determined constant.

The variations of P_m/σ_R ratio with n are shown in Fig. 6. The value of P_m/σ_R ratio is almost constant only when the pile-up/sink-in behavior is taken into account; it varies significantly between about 2.6 and 3.4 in other cases. The result of $P_m/\sigma_R \approx 3$ for steels in our study agrees well with the results obtained from the traditional optical method of residual imprint [13,19]. If this simple relation is valid for various steels, the usefulness of indentation as a substitute for tensile test will be greatly improved. Therefore, the incorporation of pile-up/sink-in effect is essential to determining the real contact between the indenter and the specimen.

The measured indentation load–depth curves of a fused quartz are shown in Fig. 7; reproducibility is good. The tip blunting was carefully examined using the condition that the elastic modulus is constant regardless of indentation depth. Then, we compared the data of contact area obtained using this condition with those calculated on various indenter radii, shown in Fig. 8. The radius of a cone indenter with 60° apex angle could be determined as 1700 nm at depth range less than 80 nm.

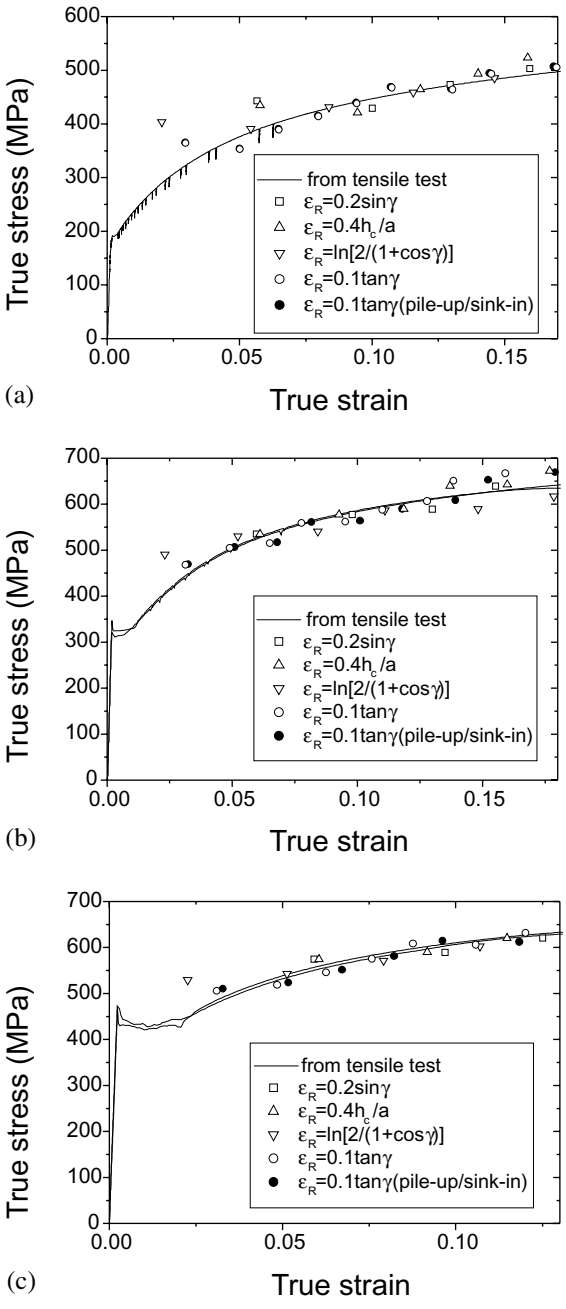

Fig. 5. Comparisons between flow properties derived from indentation load–depth curve and those from tensile test for (a) AISI1025, (b) SA106, and (c) TMCP steels.

Based on the experimental results on bulk materials and the calibration of indenter, the flow properties of Au thin films with thickness of 0.56 and 0.99 μm were derived by setting $\varepsilon_R = 0.1\tan\gamma$ and $P_m/\sigma_R = 3$, shown in Fig. 9. The averaged elastic moduli of Au films with thickness of 0.56 and 0.99 μm were determined as 133 ± 10 and 112 ± 9 GPa, respectively, and their averaged yield strengths were determined as 261 ± 30 and 154 ± 18 MPa, respectively.

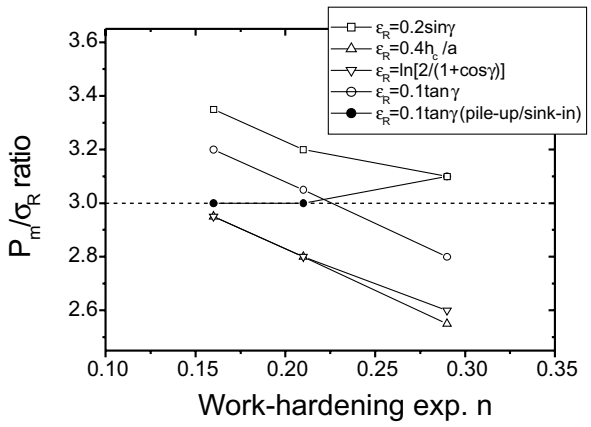

Fig. 6. The relationship between P_m/σ_R ratio and work-hardening exponent n calculated from continuous indentation test.

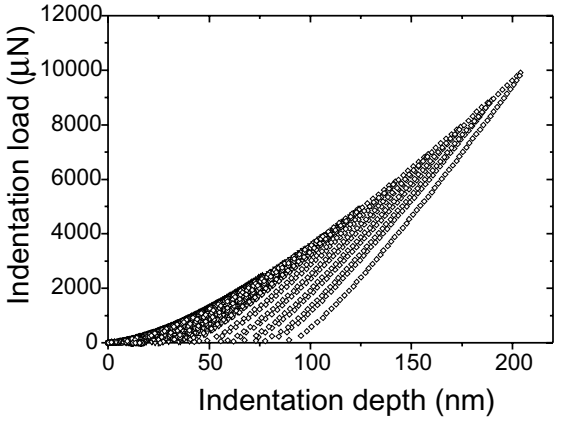

Fig. 7. Measured *P–h* curves of a fused quartz at various loads showing good reproducibility.

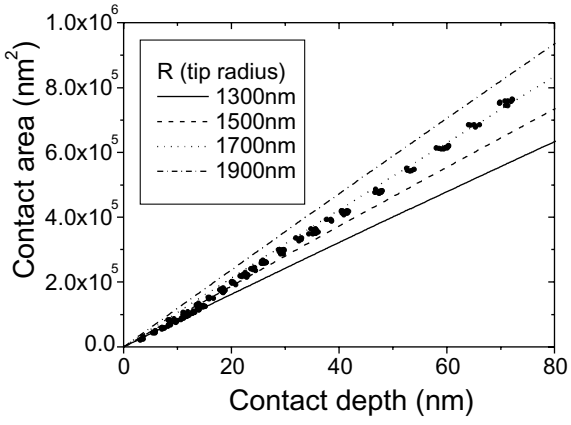

Fig. 8. Variations of contact area with contact depth, which contains the data obtained from the experimental results on a fused quartz (ℓ) and the others calculated on various indenter radii.

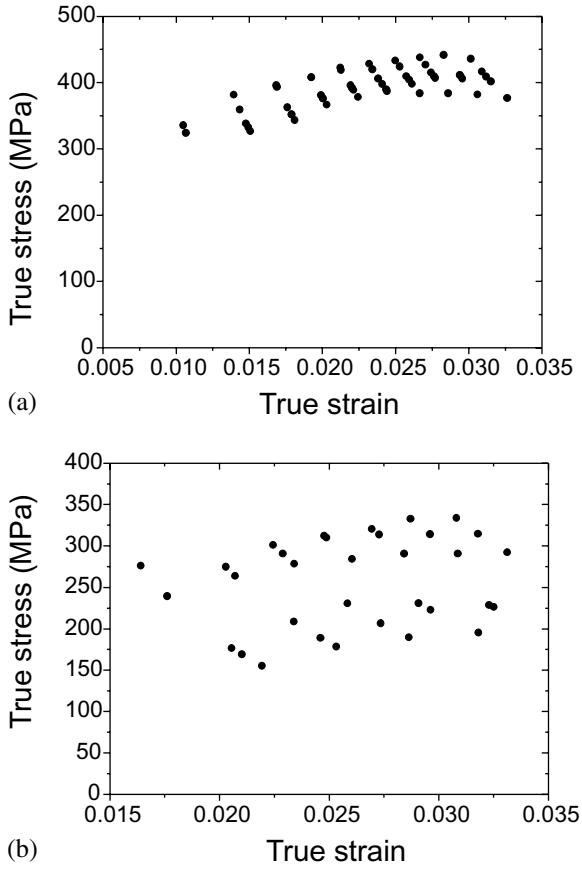

Fig. 9. The flow properties of Au thin films with thickness of (a) 0.56 and (b) 0.99 μm.

5. Conclusions

Based on the experimental results of bulk materials and the tip shape calibration at very low depth range (within about 80 nm in our experiments), the flow properties of Au thin films were derived from the indentation load–depth curve obtained by nanoindentation technique.

(1) The contact radius was determined from indentation load–depth curve. Then, the magnitude of elastic deflection was obtained by analyzing the unloading curve and the effect of pile-up/sink-in was incorporated using work-hardening exponent.
(2) Various definitions of representative strain were attempted: $0.2\sin\gamma$, $0.4h/a$, $\ln(2/(1+\cos\gamma))$, and $0.1\tan\gamma$. As a result, the shear strain at contact edge ($\tan\gamma$) was proven to be the best expression for the work-hardening characteristics of material.
(3) The value of P_m/σ_R ratio was almost constant, about 3 when the effect of pile-up/sink-in was taken into account. This agrees well with the results from the traditional optical method of residual imprint, which makes our analysis very powerful.

(4) The averaged yield strengths of Au films with thickness of 0.56 and 0.99 μm were determined as 261 ± 30 and 154 ± 18 MPa, respectively, which shows that our study is very powerful in evaluating the mechanical properties of extremely small volumes such as thin films.

References

[1] M.F. Doerner, W.D. Nix, J. Mater. Res. 1 (4) (1986) 601.
[2] W.C. Oliver, G.M. Pharr, J. Mater. Res. 7 (6) (1992) 1564.
[3] M. Sakai, Acta Metall. Mater. 41 (6) (1993) 1751.
[4] F. Yang, J.C.M. Li, Scripta Metall. Mater. 32 (1) (1995) 139.
[5] O. Prakash, D.R.H. Jones, Acta Mater. 44 (3) (1996) 891.
[6] D.S. Harding, W.C. Oliver, G.M. Pharr, Mater. Res. Symp. Proc. 356 (1995) 663.
[7] X. Li, B. Bhushan, Thin Solid Films 315 (1998) 214.
[8] S. Alba, J.L. Loubet, L. Vovelle, J. Adhes. Sci. Technol. 7 (2) (1993) 131.
[9] G. Dehm, M. Rühle, H.D. Conway, R. Raj, Acta Mater. 45 (2) (1997) 489.
[10] D.F. Bahr, J.W. Hoehn, N.R. Moody, W.W. Gerberich, Acta Mater. 45 (12) (1997) 5163.
[11] S.P. Baker, T.P. Weihs, Mater. Res. Soc. Symp. Proc. 308 (1993) 217.
[12] J. Menčík, M.V. Swain, Mater. Forum 18 (1994) 277.
[13] D. Tabor, The Hardness of Metals, Clarendon Press, Oxford, UK, 1951.
[14] D.M. March, Proc. R. Soc. London A 279 (1964) 420.
[15] C.-H. Mok, Exp. Mech. Feb. (1966) 87.
[16] R.A. George, S. Dinda, A.S. Kasper, Met. Progr. May (1976) 30.
[17] D. Kramer, H. Huang, M. Kriese, J. Robach, J. Nelson, A. Wright, D. Bahr, W.W. Gerberich, Acta Mater. 47 (1) (1999) 333.
[18] J.H. Underwood, G.P. O'Hara, J.J. Zalinka, Exp. Mech. Dec. (1986) 379.
[19] H.A. Francis, Trans. ASME (Series H) 9 (1976) 272.
[20] F.M. Haggag, in: W.R. Corwin, F.M. Haggag, W.L. Server (Eds.), ASTM STP 1204, American Society for Testing and Materials, Philadelphia, 1993, pp. 27–44.
[21] J.S. Field, M.V. Swain, J. Mater. Res. 10 (1) (1995) 101.
[22] A.C. Fischer-Cripps, B.R. Lawn, Acta Mater. 44 (2) (1996) 519.
[23] J. Alcalá, A.E. Giannakopoulos, S. Suresh, J. Mater. Res. 13 (5) (1998) 1390.
[24] B. Taljat, T. Zacharia, F. Kosel, Int. J. Solids Struct. 35 (33) (1998) 4411.
[25] K.L. Johnson, Contact Mechanics, Cambridge University Press, Cambridge, UK, 1985.
[26] J.R. Mattews, Acta Metall. 28 (1980) 311.
[27] R. Hill, B. Storåkers, A.B. Zdunek, Proc. R. Soc. London A 423 (1989) 301.
[28] R.B. King, Int. J. Solids Struct. 23 (12) (1987) 1657.
[29] K.L. Johnson, J. Mech. Phys. Solids 18 (1970) 115.
[30] Yu.V. Milman, B.A. Galanov, S.I. Chugunova, Acta Metall. Mater. 41 (9) (1993) 2523.